

Synthesis, Characterization, and Dielectric Properties of $\text{BaFe}_{10}(\text{Mn}^{2+}\text{Zn}^{2+}\text{Zn}^{2+})\text{O}_{19}$ Hexaferrite

A. Baykal¹ · M. Demir¹ · B. Ünal² · H. Sözeri³ · M. S. Toprak⁴

Received: 2 September 2015 / Accepted: 26 September 2015 / Published online: 9 October 2015
© Springer Science+Business Media New York 2015

Abstract Barium hexaferrite with nominal chemical composition $\text{BaMnZn}_2\text{Fe}_{10}\text{O}_{19}$ has been synthesized by sol–gel method, using polymethyl methacrylate (PMMA) as a template. Fourier transform infrared spectroscopy (FT-IR) and X-ray powder diffraction (XRD) were used for approving the formation of barium hexaferrites. In addition, transmission electron microscopy (TEM) and scanning electron microscopy (SEM) were performed to investigate the structural and morphological properties of BaM. The dielectric properties were studied by impedance measurements as a function of frequency (in the range 0.1 Hz–1 MHz). The XRD patterns confirmed the formation of single-phase magnetoplumbite with crystallite size around 73 nm. The results of dielectric parameters and conductivity measurements showed three regions with different behaviors in electrical conduction mechanism.

Keywords Substituted barium hexaferrite · Dielectric property · AC conductivity · Sol–gel method

1 Introduction

M-type hexaferrites, $\text{BaFe}_{12}\text{O}_{19}$ (BaM) and $\text{SrFe}_{12}\text{O}_{19}$ (SrM), have many technological applications due to their useful magnetic properties. Hexaferrites are important ferromagnetic oxides due to their intrinsic magnetic properties, such as high values of Curie temperature (T_c), coercivity (H_c), and saturation magnetization (M_s), along with their corrosion resistance, excellent chemical stability, and low cost [1–4]. These features make them potential candidate for use in magneto-optical devices, recording media, permanent magnets, and microwave devices [10].

M-type hexaferrites are also important microwave absorbing materials. Since they are magnetically hard, with high H_c and magnetic permeability, and contain a high magnetocrystalline anisotropy.

These ferrites have been synthesized by various techniques and using different compositions [4, 5]. In order to meet the requirements for specific uses, the properties of BaM ferrites are changed by replacing of cations on the Ba and Fe sites. The substitution of Ba^{2+} , Sr^{2+} [2, 3], Al^{3+} , Ga^{3+} , and Cr^{3+} [6, 7], coupled with Zn^{2+} , Co^{2+} , Mg^{2+} , Zr^{2+} , Ti^{4+} , Sn^{4+} , and Ir^{4+} substitution, can easily both modify and improve the magnetic properties (the saturation magnetization, coercivity, anisotropy constant, and ferromagnetic resonant frequency) of M-type ferrites [8–10].

✉ A. Baykal
hbaykal@fatih.edu.tr

¹ Department of Chemistry, Fatih University, B.Çekmece, 34500 Istanbul, Turkey

² Departments of Computer/Software Engineering, İstanbul Sabahattin Zaim University, Halkali-K.Çekmece, 34303 Istanbul, Turkey

³ TUBITAK-UME, National Metrology Institute, 41470 Gebze, Kocaeli, Turkey

⁴ Department of Materials and Nano Physics, KTH-Royal Institute of Technology, SE16440 Kista, Stockholm, Sweden

A variety of techniques have been used to synthesize pure and substituted $\text{BaFe}_{12}\text{O}_{19}$ particles, which include chemical coprecipitation [11], sol–gel [12], reverse microemulsion [13], ball milling [14], and sol–gel auto combustion [15] techniques. In the present work, $\text{BaMnZn}_2\text{Fe}_{10}\text{O}_{19}$ nanoparticles have been synthesized by sol–gel method using polymethyl methacrylate (PMMA) as a template. The effect of Mn–Zn substitution on the electrical properties of barium hexaferrite has been discussed.

2 Experimental

2.1 Chemicals

Iron (II) oxide nonahydrate, $\text{Fe}(\text{NO}_3)_2 \cdot 9\text{H}_2\text{O}$; barium nitrate, $\text{Ba}(\text{NO}_3)_2$; zinc nitrate, $\text{Zn}(\text{NO}_3)_2 \cdot 4\text{H}_2\text{O}$; manganese nitrate, $\text{Mn}(\text{NO}_3)_2 \cdot x\text{H}_2\text{O}$; NH_3 solution; citric acid ($\text{C}_6\text{H}_8\text{O}_7$); and PMMA ($\text{C}_5\text{O}_2\text{H}_8$)_n were obtained from Merck and used without further purification.

2.2 Instruments

Bruker D2, X'pert Pro Diffractometer which is operated at 40-kV voltage and 250-mA current using $\text{Cu K}\alpha$ radiation ($\lambda = 1.547 \text{ \AA}$) was used for X-ray powder diffraction (XRD) analysis.

Fourier transform analysis was performed by using Mattson Satellite spectrometer in the range of 4000–400 cm^{-1} in order to investigate the nature of chemical bonds formed.

Scanning electron microscopy (SEM) and transmission electron microscopy (TEM) analysis were performed

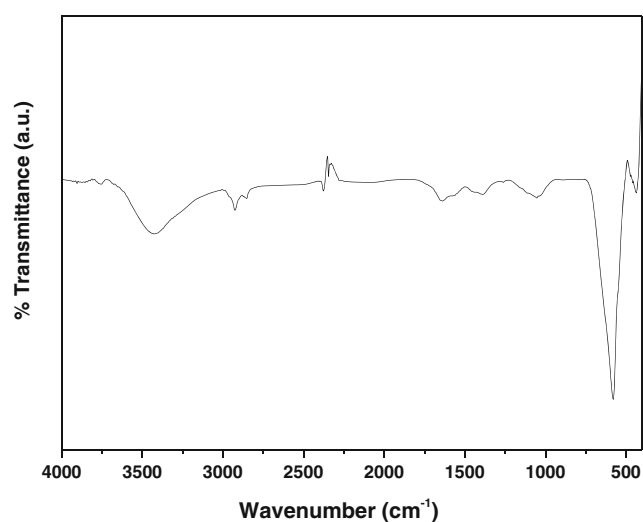


Fig. 1 FT-IR spectra of synthesized $\text{BaFe}_{10}(\text{Mn}^{2+}\text{Zn}^{2+}\text{Zn}^{2+})\text{O}_{19}$ NPs after calcination at 850 °C for 1 h

using FEI XL40 Sirion FEG and FEI Tecnai G2 Sphera microscope to study the surface morphology, particle size, and aggregation of grains, respectively.

The real (ϵ') and imaginary (ϵ'') parts of complex dielectric permittivity $\epsilon^* [= \epsilon'(\omega) + i\epsilon''(\omega)]$ were measured with a Novocontrol dielectric impedance analyzer. The dielectric data (ϵ' , ϵ'') were collected during heating as a function of frequency. The films were sandwiched between gold blocking electrodes and the conductivities were measured in the frequency range 0.1 Hz to 1 MHz at 10 °C intervals. The temperature was controlled with a Novocontrol cryosystem between –100 and 250 °C.

2.3 Procedure

For typical synthesis of the product, certain amounts of $\text{Fe}(\text{NO}_3)_2 \cdot 9\text{H}_2\text{O}$ and $\text{Ba}(\text{NO}_3)_2$ were dissolved in deionized water followed by the addition of citric acid, and its pH was adjusted to 7 by using NH_3 solution. Then, the solution was slowly concentrated at 80 °C for about 1 h and PMMA was added into the precursor solution. After ultrasonic vibration for 10 min, the mixed solution was evaporated at 70 °C till a viscous gel formed which was dried at 110 °C and finally calcined at 850 °C for 1 h [16].

3 Results and Discussions

3.1 Fourier Transform Infrared Spectroscopy Analysis

The Fourier transform infrared spectroscopy (FT-IR) spectra of calcined Ba hexaferrite sample [$\text{BaFe}_{10}(\text{Mn}^{2+}\text{Zn}^{2+}\text{Zn}^{2+})\text{O}_{19}$] is presented in Fig. 1. There are characteristic bands for ferrites observed for the

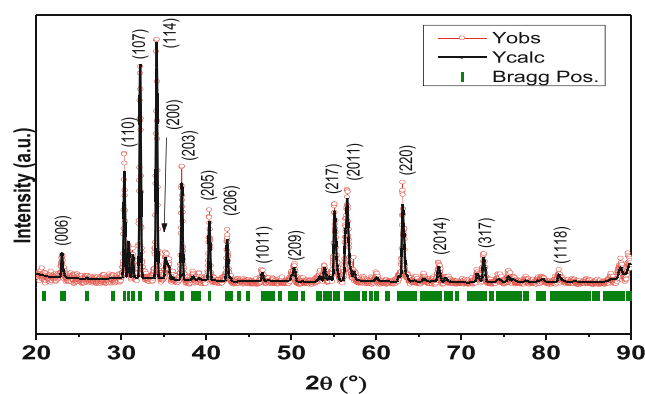


Fig. 2 XRD powder pattern of $\text{BaFe}_{10}(\text{Mn}^{2+}\text{Zn}^{2+}\text{Zn}^{2+})\text{O}_{19}$ NPs, indexed with JCPDS card no.: 84-0757, along with the simulated pattern using Rietveld analysis

sample. The strong absorbing bands appeared at around 591 and 438 cm^{-1} corresponding to typical Fe–O stretching vibration bands in $\text{BaFe}_{10}(\text{Mn}^{2+}\text{Zn}^{2+}\text{Zn}^{2+})\text{O}_{19}$ [17–19]. Small band near 2900 cm^{-1} occurs due to the presence of moisture absorbed by the sample.

3.2 XRD Analysis

Figure 2 shows the Rietveld refinement of XRD data of the product. In Fig. 2, the red spheres represent experimental data; the black solid line is calculated values by using Rietveld method. Results show that the calculated values are in good accordance with experimental data. All the peaks in Fig. 2 could be indexed to M-type hexagonal structure. XRD powder pattern of the product was in good agreement with JCPDS cards no.: 84-0757 [20, 21]. The lattice parameters and average crystallite size (based on the Scherrer formula) were calculated as $a = b = 5.889 \text{ \AA}$, $c = 23.197 \text{ \AA}$, and as 73 nm, respectively.

3.3 SEM and TEM Analysis

SEM micrograph and TEM images of the product are presented in Fig. 3a–c, respectively. Figure 3a shows the aggregation/agglomeration of nanoparticles into sheet-like structures. A closer examination using TEM revealed irregular-shaped and aggregated nanoparticles forming large sheets. There are round-shaped particles in the range of 50–300 nm,

as well as nanorod-like high aspect ratio nanoparticles with a diameter of 30–50 nm and a length of 60–300 nm observed in the micrographs. The strong aggregation is attributed to the calcination process which could generate high temperatures due to the combustion of the polymer.

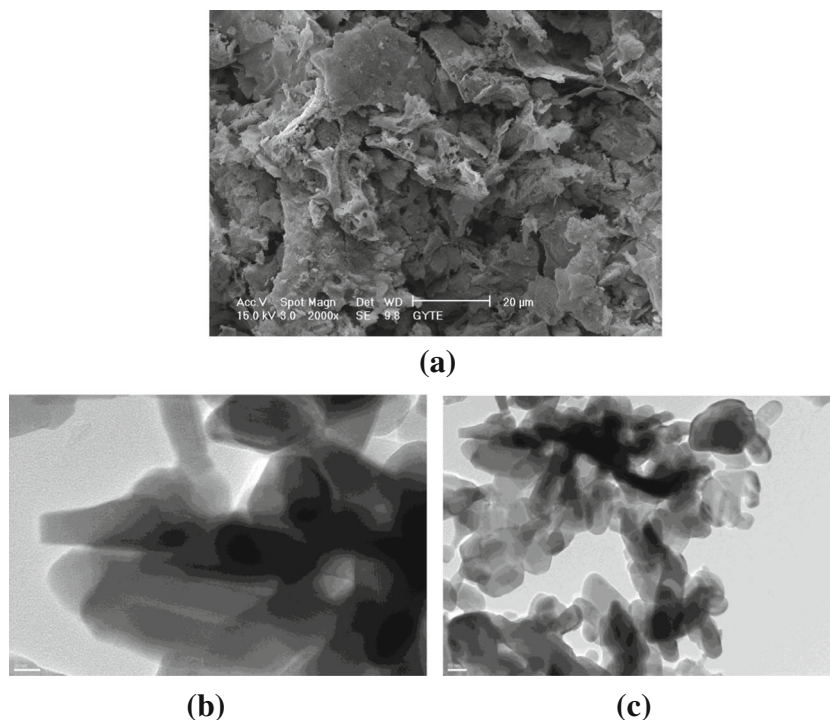
3.4 Electrical and Dielectric Analysis

Most of heterogeneous materials (polymers and composites of differently sized structures) represent both conductive and dielectric (insulating) phases. Many of these systems, together with ferroelectric polymers and composites [22–25], present a very similar frequency dependency of conductivity and permittivity, often named universal dielectric response by Jonscher [26]; its behavior is completely similar to that of Fig. 4. A typical universal dielectric response is that at lower frequency ac conductivity is frequency independent, especially above 90 °C; however at higher frequencies it increases by obeying the following power law behavior as

$$\sigma(\omega) = \sigma_0 \omega^n \quad (1)$$

The overall response can often be described by $\sigma(\omega) = \sigma_0 + A\omega^n$ where ω is the angular frequency and $n(0.6 < n < 1.0)$ and A are the temperature-dependent constants. The real part of the permittivity (ϵ') can also be expressed by a power law decay [27] such that, $\epsilon' \propto \omega^{-m}$ where m can be $1-n$.

Fig. 3 a SEM and b, c TEM micrographs of as-synthesized $\text{BaFe}_{10}(\text{Mn}^{2+}\text{Zn}^{2+}\text{Zn}^{2+})\text{O}_{19}$ NPs



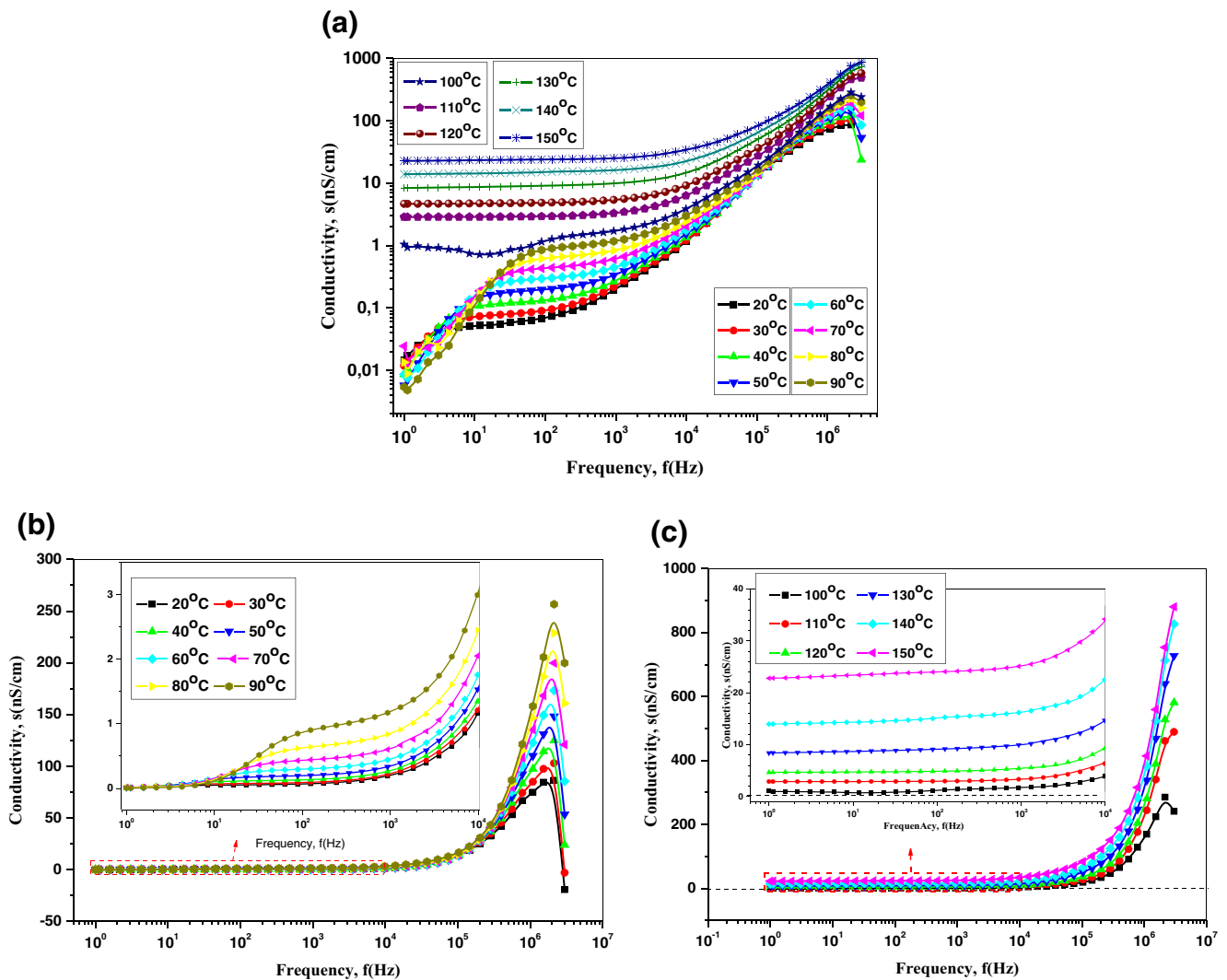


Fig. 4 **a** Conductivity analysis of as-synthesized BaFe₁₀(Mn²⁺Zn²⁺Zn²⁺)O₁₉ NPs as a function of frequency at different temperatures. **b, c** A detailed semilog representation of **a** according to the transition temperature region below and above 95 °C

3.4.1 AC Conductivity

The frequency-dependent conductivity graphs of the sample are shown in Fig. 4a. The ac conductivity value was obtained from the following standard equation, (2):

$$\sigma'(\omega) = \sigma_{ac}(\omega) = \varepsilon''(\omega)\omega\varepsilon_0 \tag{2}$$

where $\sigma'(\omega)$ is the real part of ac conductivity, $\omega(= 2\pi f)$ is the angular frequency of the signal applied across the sample, ε'' is the imaginary part of complex dielectric permittivity (ε^*), and $\varepsilon_0(= 8.852 \times 10^{-14}$ F/cm) is the vacuum permittivity.

Conductivity analysis of as-synthesized BaFe₁₀(Mn²⁺Zn²⁺Zn²⁺)O₁₉ samples represents two types of characteristic behavior depending upon temperature range before and after 95 °C. At higher temperature and higher frequency, ac conductivity complies with the rule of power law given as

$$\sigma(\omega) = \sigma_0\omega^n \tag{3}$$

where $\omega = 2\pi f$, while at lower temperature it represents a variety of trends, which can be examined in three regions as follows: (i) the first is the twisted section where the region is both frequency- and temperature-dependent. The ac conductivity of lower frequency dependency increases almost linearly up to 1–40 Hz depending upon temperature

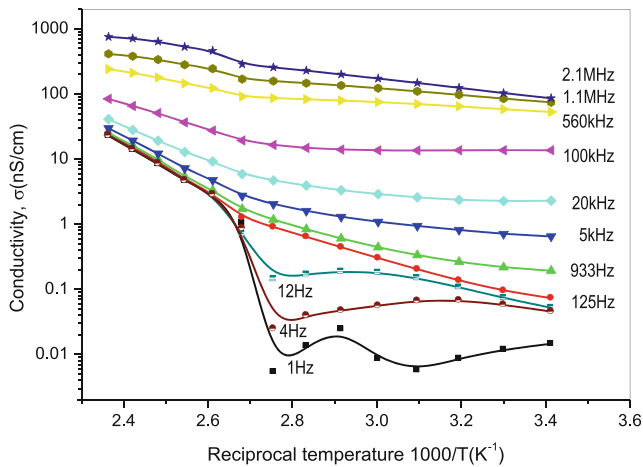


Fig. 5 Arrhenius plot of as-synthesized $BaFe_{10}(Mn^{2+}Zn^{2+}Zn^{2+})O_{19}$ NPs as a function of the reciprocal temperature at various frequencies

as shown in Fig. 4a, b but linearity extend up to 40 Hz for 90 °C.

In other words, it is found to possess almost frequency independency up to 1 kHz. (ii) The second region, temperature-dependent region only, in which conductivity increases with the elevated temperature, including higher temperature with a frequency up to 20 kHz. (iii) The third region obeys the power law, in which starting point of the ac conductivity of frequency dependency is found to shift to higher frequency while temperature is increased up to 150 °C.

Arrhenius plots of conductivity for frequencies up to 2.1 MHz show that conductivity increases with both frequency and temperature except for some fluctuation in conductivity for lower frequency (1, 4, and 12 Hz) and up to medium temperature as illustrated in Fig. 5. DC conductivity can be considered to have multiple activation energy region; however, once the frequency is increased, Arrhenius

plot for each curve over 100 Hz showed that the plot obey the well-known exponential rule as follows

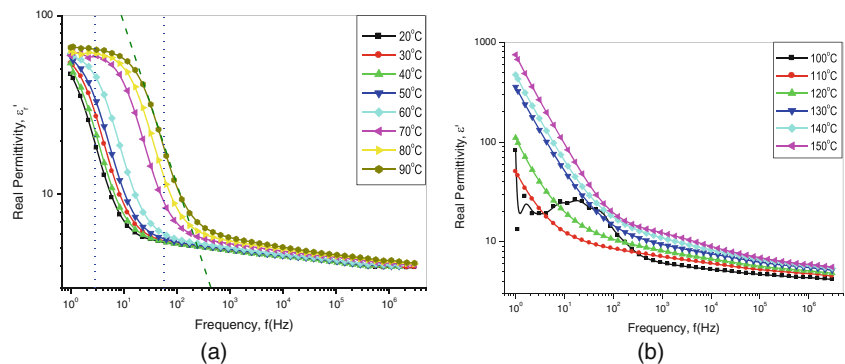
$$\sigma(T) = \sigma_0 \exp\left(-\frac{E_a}{k_B T}\right) \tag{4}$$

and can be characterized with two activation region while more than two under 100 Hz conductivity.

3.4.2 Dielectric Properties

It can be clearly seen from Fig. 6 that the dielectric constant (ϵ') decreases with increasing frequency and then reaches a constant value with two different tendencies in a certain temperature region. This behavior is expected for ferrites and is attributed to the interfacial polarization (space charge polarization) (by Maxwell–Wagner model) [28, 29]. This model states that the dielectric structure of ferrites is assumed to be made up of two layers. The first layer, being a conducting layer, contains large number of grains and the other layer consists of grain boundaries that are poor conductors. The polarization in ferrites is via a mechanism similar to the conduction process i.e., by electron exchange between Fe^{2+} and Fe^{3+} . The decrease in polarization with frequency is due to increase in the frequency of externally applied electric field, and as a result, the electron exchange between Fe^{3+} and Fe^{2+} ions cannot follow the frequency of the applied alternating field. The higher values of dielectric constant at lower frequency are due to voids, dislocations, and other defects [30]. According to Koop’s model, the dielectric constant at lower frequency comes from the grain boundary which has a high dielectric constant due to high resistivity at grain boundary. The dielectric constant at higher frequency comes from the grains which have small dielectric constant values due to low resistivity. High

Fig. 6 Real part of permittivity (ϵ_s') (dielectric constant) analysis of as-synthesized $BaFe_{10}(Mn^{2+}Zn^{2+}Zn^{2+})O_{19}$ at **a** below 90 °C and **b** above 90 °C



dielectric constants decrease the penetration depth of the electromagnetic waves by increasing the skin effect. Hence, the much lower dielectric constants obtained for the ferrites ensure their application at high frequencies.

The dielectric loss as a function of frequency for the sample is depicted in Fig. 7. The dielectric loss profiles are similar to those of the real part of dielectric constant, and additionally, ac conductivity profiles give some more information according to the regional transition as a function of both temperature and frequency. Hudson [31] has shown that the dielectric losses in ferrite are generally reflected in the conductivity measurements where the materials of high conductivity exhibit high losses and vice versa.

3.4.3 Tangent Loss Measurements

Tangent loss analysis of as-synthesized $\text{BaFe}_{10}(\text{Mn}^{2+}\text{Zn}^{2+}\text{Zn}^{2+})\text{O}_{19}$ NPs is examined and classified into three regions according to both current conduction and field propagation in Fig. 8. When the loss is about unity, lossy conduction mechanism can be dominant under the condition of a given temperature and frequency region. According to Koop's model, the lossy mechanism at lower frequency comes from the grain boundary which has a high dielectric constant due to high resistivity at grain boundary. However, at higher temperature, tangent loss represents properties of high conductivity materials as shown in Fig. 8 over a loss (%) of 10 up to 100 with a field propagation of high loss

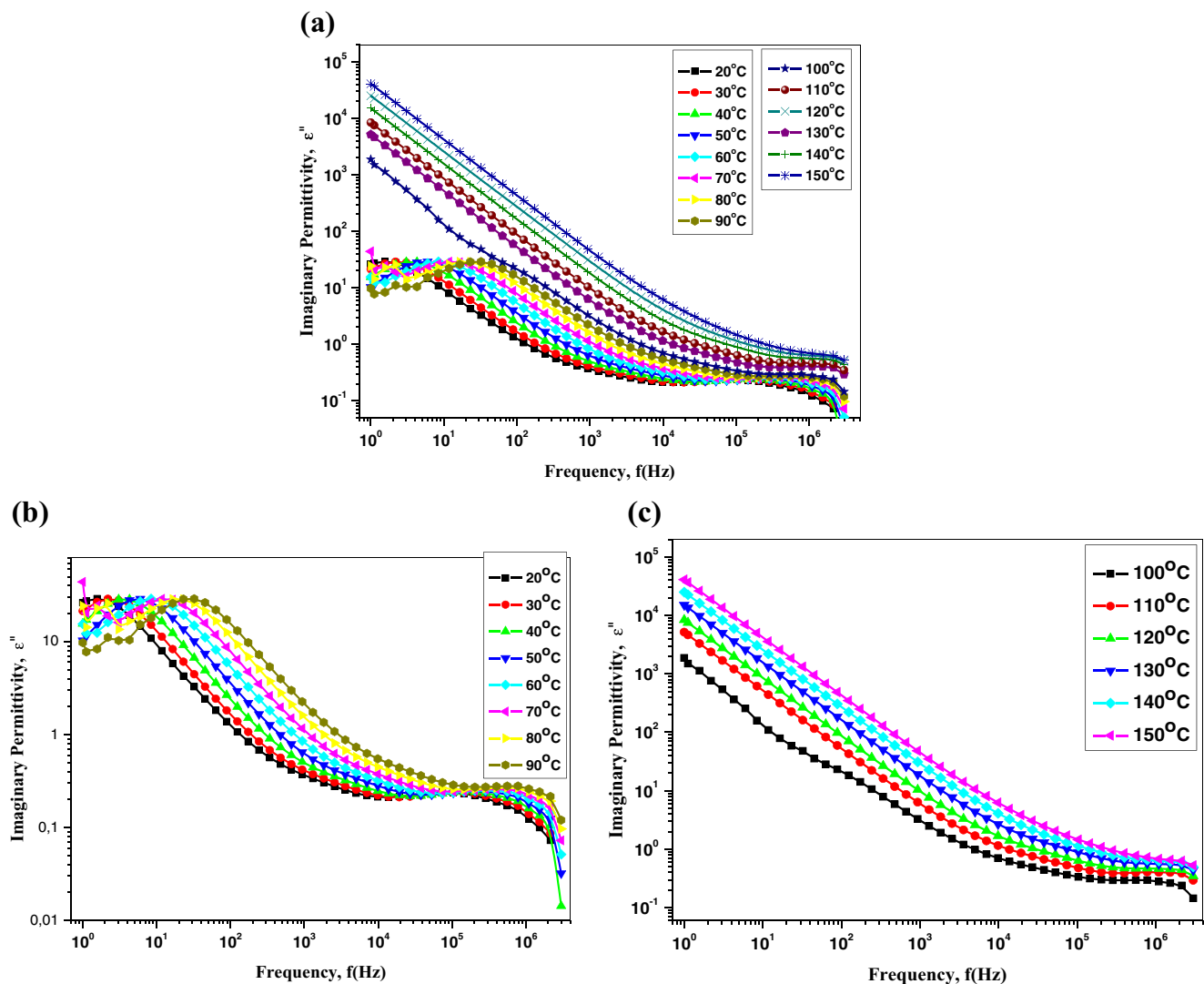


Fig. 7 a Imaginary part of permittivity (dielectric loss) analysis of as-synthesized $\text{BaFe}_{10}(\text{Mn}^{2+}\text{Zn}^{2+}\text{Zn}^{2+})\text{O}_{19}$ NPs which is also classified into two regions at b low and c high temperature

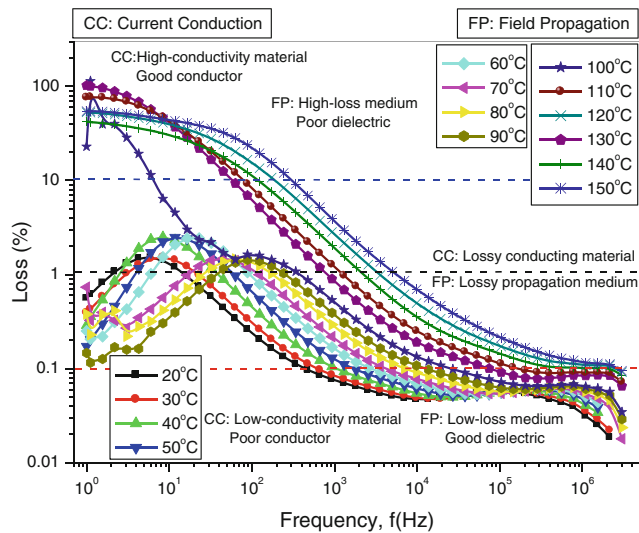


Fig. 8 Tangent loss analysis of as-synthesized $\text{BaFe}_{10}(\text{Mn}^{2+}\text{Zn}^{2+}\text{Zn}^{2+})\text{O}_{19}$ NPs as a function of frequency at various temperatures, up to 150 °C

medium of as-synthesized $\text{BaFe}_{10}(\text{Mn}^{2+}\text{Zn}^{2+}\text{Zn}^{2+})\text{O}_{19}$ grains. Poor conduction can be seen under a loss (%) of 0.1 because of small dielectric constant at higher frequency and also due to low resistivity.

4 Conclusion

$\text{BaMnZn}_2\text{Fe}_{10}\text{O}_{19}$ NPs were synthesized by conventional sol–gel method. SEM micrographs reveal polydispersed particle size and morphology, mostly aggregates in the form of hexagonal sheets. The dielectric constant (ϵ') and dielectric loss factor ($\tan \delta$) decrease with frequency and are in good agreement with the dc electrical resistivity data. The characterization of electrical conductivity, dielectric constant, and dielectric loss as well as tangent loss reveal that three regions in electrical mechanism can be originated from the interfacial polarization and large number of grains causing conducting layer and also grain boundaries resulting in poor conducting region. This type of structural and electrical properties of the sample can be utilized for a variety of the built-in sensor technology within a designated region in the VLSI technology.

Acknowledgments This work was supported by Fatih University under BAP Grant no.: 10790 and in part by Swedish Research Council (VR-SRL 2013-6780).

References

- Singhal, S., Namgyal, T., Singh, J., Chandra, K., Bansal, S.: *Ceram. Int.* **37**, 1833 (2011)
- Onreabroy, W., Papato, K., Rujijanagul, G., Pengpat, K., Tunkasiri, T.: *Ceram. Int.* **38S**, S415 (2012)
- Ullah, Z., Atiq, S., Naseem, S.: *J. Alloy. Compd.* **555**, 263 (2013)
- Durmus, Z., Sozeri, H., Toprak, M.S., Baykal, A.: *Nano-Micro Letters* **3**(2), 194 (2011)
- Petrila, I., Tudorache, F.: *Superlattice Microst.* **7**, 46 (2014)
- Katlakunta, S., Meena, S.S., Srinath, S., Bououdina, M., Sandhya, R., Praveena, K.: *Mater. Res. Bull.* **63**, 58 (2015)
- Castellanos, P.A.M., Borges, A.C.M., Melgar, G.O., Garcia, J.A., Alcaide, E.G.: *Physica B* **406**, 3130 (2011)
- Ashiq, M.N., Shakoor, S., Najam-ul-Haq, M., Warsi, M.F., Ali, I., Shakir, I.: *J. Magn. Magn. Mater.* **374**, 173 (2015)
- Din, M.F., Ahmad, I., Ahmad, M., Farid, M.T., Iqbal, M.A., Mur-taza, G., Akhtar, M.N., Shakir, I., Warsi, M.F., Khan, M.A.: *J. Alloy. Compd.* **584**, 646 (2014)
- Ali, I., Islam, M.U., Awan, M.S., Ahmad, M., Ashiq, M.N., Naseem, S.: *J. Alloy. Compd.* **550**, 564 (2013)
- Willis, A.L., Turro, N.J., O'Brien, S.: *Chem. Mater.* **17**, 5970 (2005)
- Zhang, H.J., Yao, X., Zhang, L.Y.: *Mater. Sci. Eng.* **84**, 252 (2001)
- Li, L., Chen, K., Liu, H., Tong, G., Qian, H., Hao, B.: *J. Alloy. Compd.* **557**, 11 (2013)
- Topal, U., Ozkan, H., Dorosinskii, L.: *J. Alloy. Compd.* **428**, 17 (2007)
- Mandizadeh, S., Soofivand, F., Salavati-Niasari, M., Bagheri, S.: *J. Ind. Eng. Chem.* **26**, 167 (2015)
- Mu, G., Chen, N., Pan, X., Shen, H., Gu, M.: *Mater. Lett.* **62**, 840 (2008)
- Carreno, T.G., Morales, M.P., Serna, C.J.: *Mater. Lett.* **43**, 97 (2000)
- Birsöz, B., Baykal, A., Sözeri, H., Toprak, M.S.: *J. Alloy. Compd.* **493**, 481 (2010)
- Baykal, A.: *J. Supercond. Nov. Magn.* **27**, 877 (2014)
- Sözeri, H., Baykal, A., Ünal, B.: *Phys. Status Solidi A* **209**, 2002 (2012)
- Sözeri, H., Mehmedi, Z., Kavas, H., Baykal, A.: *Ceram. Int.* **41**, 9602–9609 (2015)
- Panteny, S., Stevens, R., Bowen, C.R.: *Ferroelectrics* **319**, 199 (2005)
- James, A.R., Priya, S., Uchino, K., Srinivas, K.: *J. Appl. Phys.* **90**, 3504–3508 (2001)
- Neagu, R.M., Neagu, E., Bonanos, N., Pissis, P.: *J. Appl. Phys.* **88**, 6669 (2000)
- Furukawa, T., Yasuda, K., Takahashi, T.: *IEEE T. Dielect. El. In.* **11**, 65 (2004)
- Jonscher, A.K.: *Nature* **253**, 717–719 (1975)
- Bobnar, V., Lunkenheimer, P., Henberger, J., Loidl, A., Lichtenberg, F., Mannhart, J.: *Phys. Rev. Lett.* **65**, 155115 (2002)
- Wagner, K.W.: *Ann. Phys.* **345**, 817 (1913)
- Maxwell, J.C.: Oxford University Press, Oxford (1929). section 328
- Sirdeshmukh, L., Kumar, K.K., Laxman, S.B., Krishna, A.R., Sathaiyah, G.: *B. Mater. Sci.* **21**, 219 (1998)
- Hudson, A.S.: *Marconi Review* **37**, 43 (1968)